Title

Homogenized halides and alkali cation segregation in alloyed organic-inorganic perovskites.

Journal

Science (New York, N.Y.), 363(6427)

ISSN

0036-8075

Authors

Correa-Baena, Juan-Pablo
Luo, Yanqi
Brenner, Thomas M
et al.

Publication Date

2019-02-01

DOI

10.1126/science.aah5065

Peer reviewed

SOLAR CELLS

Homogenized halides and alkali cation segregation in alloyed organic-inorganic perovskites

Juan-Pablo Correa-Baena[1,2]*†, Yanqi Luo[3,4]†, Thomas M. Brenner[3,4]‡, Jordan Snaider[5], Shijing Sun[1], Xueying Li[4,6], Mallory A. Jensen[1], Noor Titan Putri Hartono[1], Lea Nienhaus[1], Sarah Wieghold[1], Jeremy R. Poindexter[1], Shen Wang[3,4], Ying Shirley Meng[3,4], Ti Wang[5], Barry Lai[7], Martin V. Holt[8], Zhonghou Cai[7], Moungi G. Bawendi[1], Libai Huang[5], Tonio Buonassisi[1]*, David P. Fenning[3,4,6]*

The role of the alkali metal cations in halide perovskite solar cells is not well understood. Using synchrotron-based nano–x-ray fluorescence and complementary measurements, we found that the halide distribution becomes homogenized upon addition of cesium iodide, either alone or with rubidium iodide, for substoichiometric, stoichiometric, and overstoichiometric preparations, where the lead halide is varied with respect to organic halide precursors. Halide homogenization coincides with long-lived charge carrier decays, spatially homogeneous carrier dynamics (as visualized by ultrafast microscopy), and improved photovoltaic device performance. We found that rubidium and potassium phase-segregate in highly concentrated clusters. Alkali metals are beneficial at low concentrations, where they homogenize the halide distribution, but at higher concentrations, they form recombination-active second-phase clusters.

The highest reported power conversion efficiencies (PCEs) for lead halide perovskite solar cells (PSCs) have been achieved with mixed methylammonium (MA) and formamidinium (FA) A-site cations and mixed Br and I X-site anions (*1*–*4*). Tuning the stoichiometry of the organic to the inorganic ions is critical for achieving high photocurrents (*5*). Cs has been used as the A-site cation to explore more complex compositions, including Cs and MA, Cs and FA, and Cs, MA, and FA (*1*, *6*–*10*). Similarly, adding Rb into a multi-cation perovskite improved efficiency (*11*, *12*) and enhanced device stability at elevated temperatures of 85°C (*11*). The improved performance may be the result of increased charge carrier lifetime and mobility (*13*). More recently, K was also used to improve the stabilized PCE of PSCs (*14*, *15*).

Despite these impressive results, the mechanisms that form the basis for improved electronic properties, performance, and stability upon changes in the precursor stoichiometry and the addition of alkali metals are not yet well understood. Past work hinted at the suppression of low-dimensional wide–band gap polymorphs, which may act as recombination-active sites (*8*, *11*, *13*). In addition, previous studies with bulk techniques (*6*–*8*, *11*, *14*) averaged over large areas (0.2 to 1 cm^2) may have overlooked minority-phase formation and elemental agglomeration at the nanoscale.

We used mapping techniques with nanoscale resolution to elucidate the elemental distribution of the alkali metals and their relation to electronic properties and device performance. Synchrotron-based nanoscale x-ray fluorescence (n-XRF) mapped the elemental distribution in multi-ion perovskites. Where alkali metals were added, the halide distribution became homogeneous for films with excess lead halide precursor. Transient absorption spectroscopy mapping showed that perovskite films without addition of alkali metal iodides (and with segregated halides) had greater heterogeneity in the charge carrier dynamics than those with CsI, RbI, or both. Also, Rb and K could segregate into large clusters. When the alkali metal additives exceeded 1%, we observed second-phase alkali metal–rich aggregates that induce charge carrier recombination at Rb-rich clusters.

In addition to the perovskite films with 10% excess PbI_2 and $PbBr_2$ [overstoichiometric (OSt)], we prepared samples containing no excess (St) and with deficient lead halide precursor stoichiometry [substoichiometric (SSt)] with respect to the organic cations MA and FA. These perovskites have a composition of $(MAPbBr_3)_{0.17}(FAPbI_3)_{0.83}$, similar to those previously studied (*2*, *11*). We added 5% CsI, 5% RbI, 5% CsI and 5% RbI, or 5% KI with respect to the PbI_2 (see table S1 for details on compositions) for the OSt, St, and SSt samples, which we refer to as Cs-I/Br, Rb-I/Br, RbCs-I/Br, and K-I/Br, respectively. FAI and MAI were also added to understand the effect of adding additional organic cations to the OSt solutions. Perovskite thin films were prepared with the combinations X-I/Br, where X is the alkali metal added (or FAMA) and I/Br refers to the baseline perovskites.

Solar cells were prepared with a typical device structure (Fig. 1A; see supplementary materials). A transmission electron microscopy (TEM) cross-sectional image is shown for a PSC with I/Br (Fig. 1B) perovskite [see fig. S1 for scanning electron microscopy (SEM) cross-sectional images of several compositions]. Representative current density–voltage (*J-V*) curves, including the backward and forward scans, for OSt I/Br and top performer RbCs-I/Br are shown in Fig. 1, C and D, respectively. The champion device for the I/Br perovskites yielded an open-circuit voltage (V_{OC}) of 1.09 V, short-circuit current density (J_{SC}) of 22.8 mA/cm^2, fill factor (FF) of 51%, and PCE of 12.6% under AM1.5 illumination. In contrast, the champion device prepared with RbCs-I/Br yielded V_{OC} = 1.10 V, J_{SC} = 22.7 mA/cm^2, FF = 76%, and PCE = 19%. The parameters were extracted from the backward scan, and no appreciable difference was observed between backward and forward scans (*11*).

The performance of device replicates for each of the studied compositions is shown in Fig. 1, E and F. For the OSt samples, V_{OC} (Fig. 1E) and performance (PCE; Fig. 1F) increased with the addition of Rb or Cs (or both) or FAMA, but decreased upon KI addition. Full device performance parameters are shown in fig. S2. The beneficial effect of cation addition has been ascribed to the reduction in concentration of the "yellow-phase" impurity of the FA-based perovskites (*7*, *8*, *16*). The time-resolved photoluminescence decay of the perovskites slowed considerably with the addition of the alkali metal iodides to the OSt perovskites (fig. S3) (*17*), in agreement with the increase in V_{OC} and other studies (*13*). The J_{SC} values of these devices remained relatively constant with perovskite composition, and FF markedly increased with the addition of alkali metal iodides, with an especially large discrepancy between I/Br and RbCs-I/Br samples (with the exception of KI; fig. S2C).

The St and SSt samples showed a very different trend. The former showed an increase in V_{OC} (Fig. 1E) and J_{SC} (fig. S2E) upon alkali metal halide addition, with the exception of RbCs-I/Br, and an unmodified FF. However, performance was lower than that of the OSt samples (Fig. 1I). The SSt samples showed an increase in V_{OC} and J_{SC} upon addition of CsI or RbI, but there was no benefit to adding KI or both RbI and CsI. All of the SSt samples showed low FF and low PCE (Fig. 1F). We ascribed this lower performance to the formation of a thick organic layer at the surface of the perovskite crystal, with a passivating effect (*5*). The highest V_{OC} and PCE values were measured for OSt samples with addition of both RbI and CsI.

[1]Massachusetts Institute of Technology, Cambridge, MA 02139, USA. [2]School of Materials Science and Engineering, Georgia Institute of Technology, Atlanta, GA 30332, USA. [3]Department of Nanoengineering, University of California, San Diego, La Jolla, CA 92093, USA. [4]Sustainable Power and Energy Center, University of California, San Diego, La Jolla, CA 92093, USA. [5]Department of Chemistry, Purdue University, West Lafayette, IN 47907, USA. [6]Materials Science and Engineering Program, University of California, San Diego, La Jolla, CA 92093, USA. [7]Advanced Photon Source, Argonne National Laboratory, Lemont, IL 60439, USA. [8]Center for Nanoscale Materials, Argonne National Laboratory, Lemont, IL 60439, USA.
***Corresponding author. Email: jpcorrea@gatech.edu (J.-P.C.-B.); buonassisi@mit.edu (T.B.); dfenning@eng.ucsd.edu (D.P.F.)**
†These authors contributed equally to this work. ‡Present address: Department of Materials and Interfaces, Weizmann Institute of Science, Rehovot 76100, Israel.

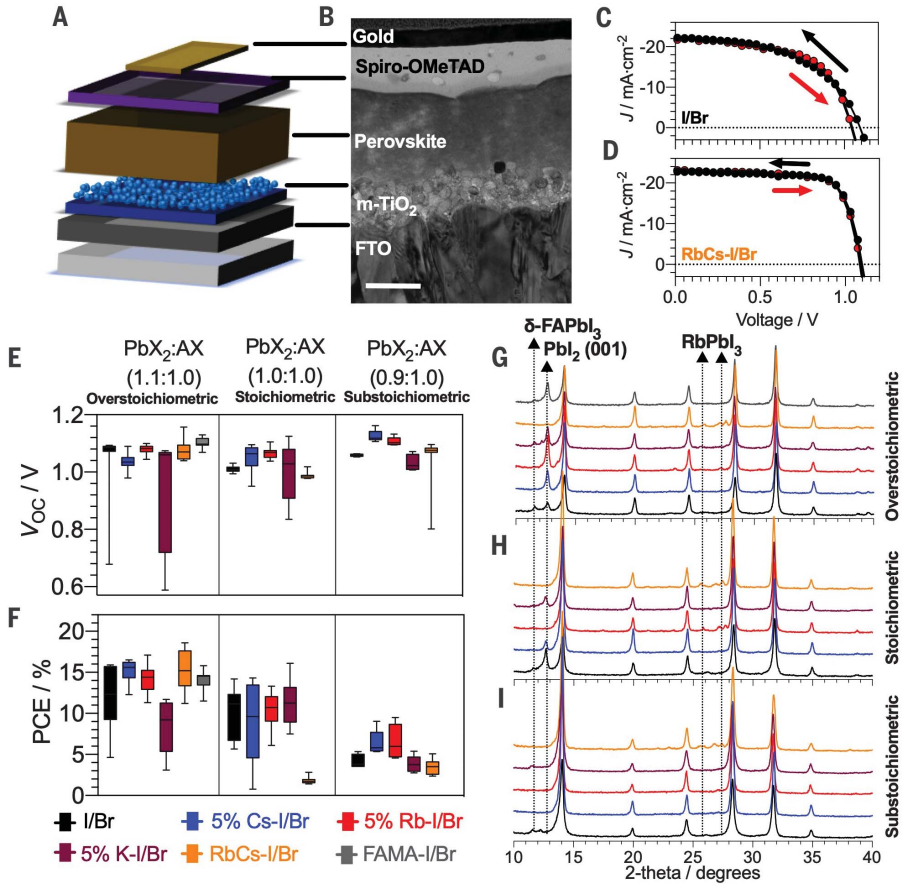

Fig. 1. Perovskite thin film and solar cell characterization. (**A**) Schematic of the perovskite solar cells studied. (**B**) Cross-sectional TEM for the RbCs-I/Br device. Scale bar, 200 nm. (**C** and **D**) Perovskite solar cell current-voltage characteristics for OSt I/Br (C) and RbCs-I/Br (D). The black and red traces are backward and forward scans, respectively. (**E** and **F**) The statistical values of up to 8 pixels (two substrates with 4 pixels each) are shown for V_{OC} (E) and PCE (F). The boxes denote, from bottom to top, the minimum, 25th percentile, median, 75th percentile, and maximum values. (**G** to **I**) Grazing incidence x-ray diffraction of perovskite thin film with overstoichiometric (G), stoichiometric (H), and substoichiometric (I) samples. Solar cell performance parameters and x-ray diffraction are measured for overstoichiometric, stoichiometric, and substoichiometric samples with the addition of CsI, RbI, KI, both CsI and RbI, and FAMA to the precursor solution.

Grazing incidence x-ray diffraction confirmed that the crystalline phases of the perovskite thin films (Fig. 1, G to I, and fig. S4) were bulk structures with cubic symmetry. We attribute the impurity peaks at low angles to small amounts of the nonperovskite one-dimensional (1D) phase of δ-$FAPbI_3$ present in the OSt and St films. The peaks between 25° and 28° were assigned to the nonperovskite 1D $RbPbI_3$ (fig. S5).

Our results confirmed that addition of RbI and CsI suppresses the formation of the PbI_2 phase. The relative peak intensity of the PbI_2 (001) peak at 12.63° decreased drastically upon addition of both RbI and CsI, with little to no effect with the addition of CsI, RbI, KI, and FAI and MAI in the OSt films (Fig. 1G). Similarly, the addition of both CsI and RbI markedly suppressed the PbI_2 peak; a more modest effect was seen with the addition of the individual alkali iodides in the St films (Fig. 1H). Samples based on the SSt perovskite showed suppression of the PbI_2 (001) peak upon addition of all alkali iodides, with a δ-$FAPbI_3$ phase remaining upon KI addition (Fig. 1I).

The addition of these alkali iodides increased the lattice constants and cell volume of the cubic perovskites (fig. S4, D to F, and table S2), indicating incorporation of the A-site cation, the large X-site halide, or both. Adding more I to these Br-containing perovskites increases their lattice parameters, as I helps to expand the lattice. Peak full width at half maximum (FWHM) analysis (fig. S6) showed that at the bulk level, the addition of small Rb and Cs cations led to a less strained lattice, and that the modified distribution of I and Br led to a more homogeneous d-spacing between various lattice planes. The incorporation of both CsI and RbI was needed to suppress undesired phases (PbI_2 and δ-$FAPbI_3$) as well as to reduce the strain in the perovskite structure, which can lead to a more stable structure (*18*).

To further understand the role of CsI, RbI, or KI addition, we performed n-XRF on all perovskites. The n-XRF resolution was limited by a 250-nm x-ray beam (FWHM at 16.3 keV). Rb K_α, I L_α, Br K_α, and Pb L_α XRF emission from the perovskite absorber was detected, but C and H in the FA and MA cations are too light to be detected. The XRD data (fig. S4) suggested that major changes occurred for RbI and CsI addition. In the n-XRF maps, all of the OSt samples exhibited Br-poor clusters (Br:Pb molar ratio less than 0.48, versus the expected molar ratio of 0.49). The Br-poor regions were selected and are shown in fig. S7 to highlight the pronounced variations (See table S3 for quantification).

The OSt I/Br perovskite, containing no alkali ions, showed large clusters of lower Br content, 6 to 8 μm in size; 41% of the scanned region was Br-poor (Fig. 2, A and N). Upon RbI or CsI addition, or both, we observed homogenization in Br (Fig. 2, B to D). The Br-poor area fraction was reduced to 32% and 29% for individual RbI and CsI addition, respectively. As a control experiment, we added FAMA to the OSt I/Br solution (Fig. 2E) and observed modestly improved homogeneity of Br. With both RbI and CsI addition, only ~6% of the total area was Br-poor (Fig. 2D), hence this combination yields the most halide homogenization. Slight halide homogenization by RbI occurred for samples containing >1% in solution (fig. S8). Addition of KI did not induce homogenization of the Br but rather formed aggregates that were Br-rich relative to the I/Br sample (fig. S9 and table S3). The distribution of I in the films was homogeneous across the different amounts and types of alkali metal iodide addition (fig. S10). We saw no evidence of changes in the halide distribution upon beam irradiation for some minutes.

To understand the effects of Br segregation on the short-lived carrier recombination dynamics of the perovskite films, we compared transient absorption microscopy (TAM) images to the n-XRF maps (fig. S11). The OSt I/Br sample showed a large range of TAM dynamics, ranging from short- to long-lived decays (fig. S12), whereas samples with added CsI and/or RbI showed much narrower distributions, as expected from the maps in fig. S11, E to H. Quantification of the n-XRF and TAM distributions provided corroborating evidence of reduced elemental and electronic heterogeneity in samples with alkali metal ion incorporation.

We analyzed St and SSt preparations and detected Br-rich cluster areas (Fig. 2, F to M). Although the Br-rich clusters were difficult to recognize visually, the St and SSt samples without CsI and RbI addition exhibited Br-rich cluster area ratios of 0.08 and 0.13, respectively (Fig. 2, O and P). Similar to the OSt samples, however, the St and SSt analogs benefited from the addition of CsI, yielding small Br-rich area ratios of 0.01 and 0.003, respectively. Br-rich aggregates were formed with the addition of RbI alone in both St

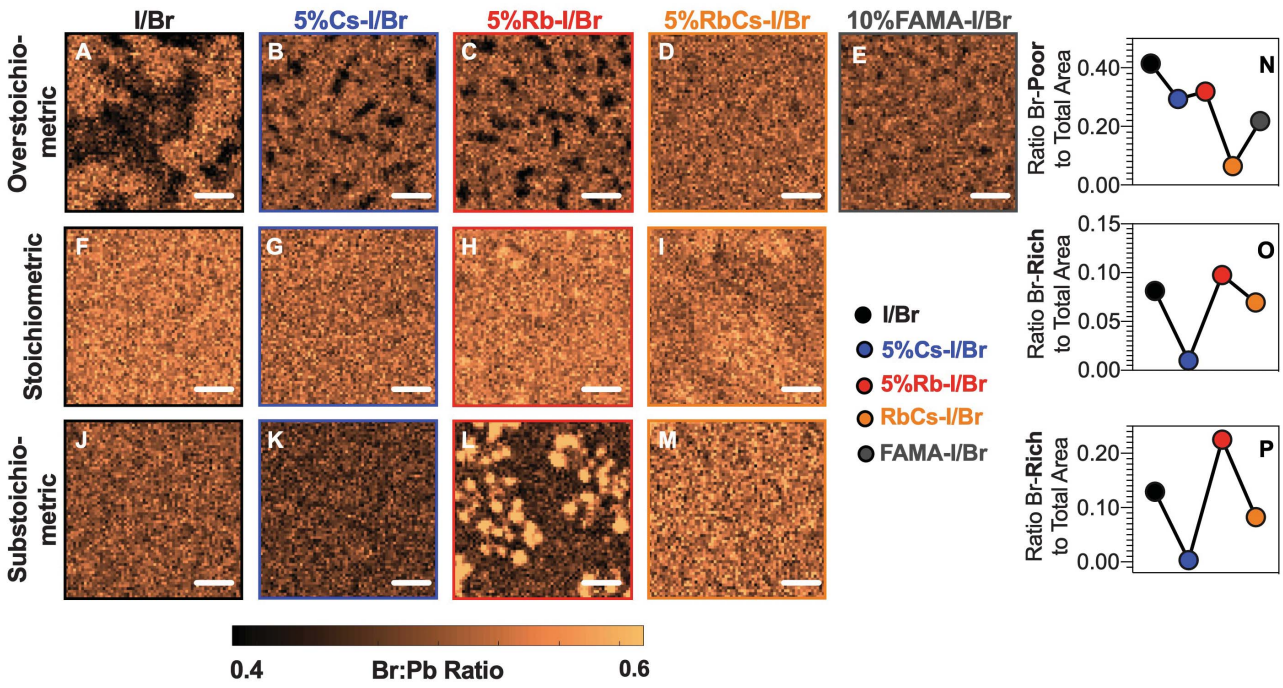

Fig. 2. Halide distribution. (**A** to **M**) X-ray fluorescence mapping indicates heterogeneous distribution of Br as a function of alkali metal incorporation and stoichiometric composition of the perovskite films. Br-poor [(A) to (E)] and Br-rich [(F) to (M)] areas are discernable. (**N**) Area fraction of the overstoichiometric Br-poor regions with respect to the whole n-XRF map. (**O** and **P**) Area fraction of the stoichiometric (O) and substoichiometric (P) Br-rich regions. Scale bars, 2 μm.

Fig. 3. Elemental distribution of Rb in perovskites of different compositions. (**A** to **C**) Rb XRF maps of the 5% Rb–added samples with different stoichiometries. (**D** to **F**) Rb XRF maps of the 5% Rb and 5% Cs–added samples with different stoichiometries. Scale bar, 5 μm.

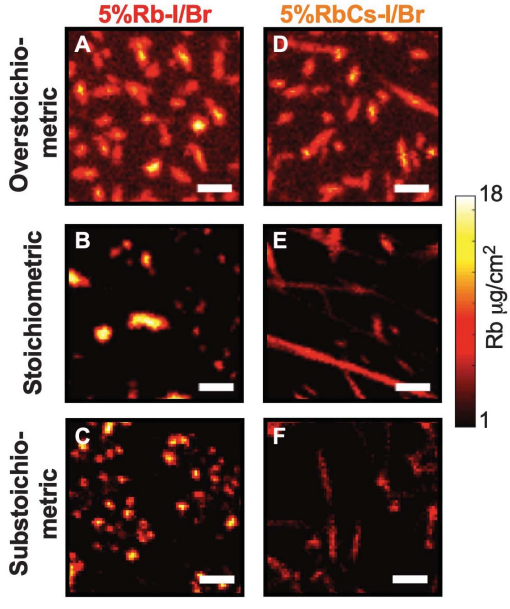

and SSt. A slight homogenization of Br was observed upon addition of RbI and CsI, yielding a smaller Br-rich area ratio of 0.07 for the St films. Similar to the St conditions, samples prepared in SSt conditions yielded identical trends of Br distribution upon alkali metal halide addition. These SSt materials yielded higher V_{OC} values and lower photocurrents than the St and OSt samples (*5*, *19*). We attribute the higher V_{OC} to the homogenization of Br, which reduced recombination-active areas. The lower photocurrent has been suggested to be the result of hindered charge extraction at the charge-selective contact and perovskite interface (*5*). These measurements confirmed the importance of addition of CsI and/or RbI for halide homogenization.

Several recent reports show that adding Rb and Cs yields higher stabilized efficiencies (*8*, *11*–*13*, *20*), and solid-state nuclear magnetic resonance experiments have provided some evidence that Rb and K are not incorporated into the lattice of the perovskite structure (*21*). We used n-XRF to map the Rb and K concentration and distribution within the perovskite absorbers in fully functional devices (Fig. 3 and fig. S13) with Ost, St, and SSt perovskites. Evaluation of the Cs elemental distribution is challenging in the I-containing perovskites because of the overlapping Cs_L and I_L XRF emission lines. We measured the Rb XRF signal (Fig. 3, A to C) for all Rb-I/Br samples; all showed large clusters of Rb, with varying sizes and distributions depending on the stoichiometry of the perovskite solution. Loading as little as 1% Rb into the perovskite precursor caused segregation of highly concentrated Rb clusters, and with a further increase in the Rb concentration, large aggregates appeared (fig. S13, A to C).

By introducing Cs (forming the composition RbCs-I/Br), the Rb aggregates changed from large precipitates to rodlike structures of lower density, especially for the St and SSt samples. Similarly, K-I/Br perovskite samples [deposited as thin films on fluorine-doped tin oxide (FTO) glass] containing varying amounts of KI showed aggregates of high concentration of K at a concentration of 5%, and needle-like structures at a concentration of 10% (fig. S13). Although some of the K and Rb may be incorporated into the film homogeneously and below the n-XRF bulk detection limits (*14*, *22*) either as constituent atoms or passivants (*15*), we observed an appreciable

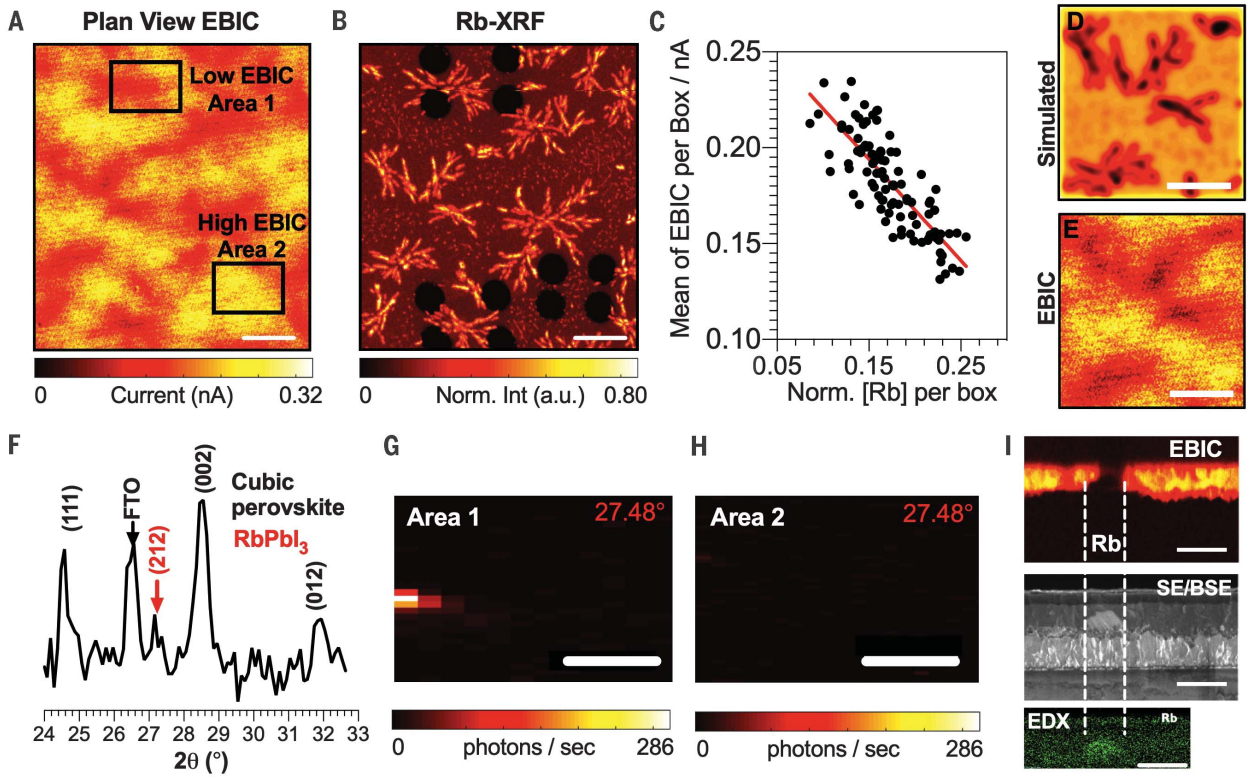

Fig. 4. The chemical nature and the electronic properties of Rb aggregates in OSt perovskites. (**A** and **B**) Plan-view EBIC profile (A) and the correlated Rb-XRF map (B) of the 5%Rb-I/Br perovskite device. Three regions are marked with focused ion beam (FIB). Area 1 and area 2 are the low- and high-EBIC regions, respectively. Scale bars, 10 μm. (**C**) Scatterplot between Rb concentration and its effect on EBIC charge collection. The individual data points are produced by taking the average within 10 × 10 square pixel boxes in (B). (**D**) The Rb XRF map convoluted with the beam generation profile and a Gaussian diffusion broadening of 600 nm. (**E**) The corresponding EBIC profile of the selected Rb XRF maps. Scale bars, 5 μm. (**F**) An x-ray diffraction pattern taken at 8 keV with 50 μm spot size in the area within the whole region shown in (A). (**G** and **H**) The scanning x-ray Bragg diffraction microscopy map for areas 1 and 2 taken at the $RbPbI_3$ Bragg condition where 2θ = 27.48°. Scale bars, 5 μm. (**I**) Cross-section EBIC, simultaneously collected SE/BSE, and corresponding EDX. Scale bars, 1 μm.

amount of the K and Rb agglomerates in large clusters.

To reveal the electronic role of these large aggregates of alkali metals in the Rb-I/Br samples, we conducted n-XRF/x-ray beam–induced current (XBIC) measurements for the devices containing different RbI concentrations (fig. S14). The in situ measurement of n-XRF/XBIC suggests that these Rb aggregates suppressed charge collection in the 5% Rb-I/Br device. However, because the XBIC showed relatively poor signal-to-noise ratio, we performed electron beam–induced current (EBIC) measurements, which provided improved images. The plan-view EBIC profile of the Rb-I/Br sample (Fig. 4A) was collected and used to create fiducial markers by focused ion beam (FIB) for subsequent n-XRF investigation (Fig. 4B).

Two distinct regions, one of lower EBIC and one of higher EBIC, are marked in Fig. 4A. In the corresponding Rb XRF map (Fig. 4B), the dark circles are the FIB markers. To assess the correlation between Rb distribution and local carrier collection, we divided the EBIC map and the normalized Rb elemental map into 10 × 10 boxes; Fig. 4C is a plot of the average value within each box of the EBIC current versus the corresponding local average Rb concentration. Figure 4C displays a negative correlation (r^2 = 0.6) between charge collection and local Rb concentration, suggesting a detrimental effect from the Rb clusters.

Current suppression in EBIC has several possible origins, including low carrier generation, current blocking, and carrier recombination-active sites. The correlative study allowed us to compare the Rb aggregate size and its current collection profile directly to evaluate whether the aggregates were recombination-active. The low-EBIC features in Fig. 4A were broader than the Rb ones in XRF. Broadening can be caused by a larger size of the carrier generation volume under the electron beam excitation relative to the n-XRF probe, by carrier diffusion away from this generation volume followed by recombination of free carriers near or at the Rb clusters, or by both effects. If the Rb aggregates were only charge-blocking and recombination-inactive, then we would expect the EBIC maps to correspond with the Rb n-XRF maps once we accounted for the smearing caused by a large carrier generation volume in EBIC. We modeled electron beam broadening by convoluting the Rb elemental distribution map with a simulated carrier generation profile under the electron beam [simulated using CASINO (*23*); see supplementary materials and fig. S15, A and C, for details, beam profile, and simulated map].

Alternatively, if the Rb aggregates were recombination-active, then their interfaces would act as a sink for diffusing excited carriers, and we would need to account for carrier diffusion to the aggregates. To model broadening caused by free carrier diffusion and recombination, we further convoluted the beam-broadened Rb map with a Gaussian diffusion profile with a diffusion length of 600 nm. Upon addition of this simulated charge carrier diffusion (Fig. 4D), the broadening of the signal approached that of the EBIC (Fig. 4E).

As a further illustration of the importance of accounting for carrier diffusion to the Rb aggregates, a randomly selected line profile is highlighted in fig. S16, A and B (blue dotted line). Modeled beam- and diffusion-broadened line profiles were plotted against the n-XRF and EBIC profiles (fig. S16C). Comparison of the profiles indicated that although strong contrast

at the n-XRF Rb features was maintained by convolution with the beam profile, this contrast was smeared out by convolution with the diffusion profile. This smearing was observed in the actual EBIC profile, indicating that carrier diffusion was critical to explaining the low-EBIC areas corresponding to Rb-rich aggregates. (See fig. S17 for quantification of the induced current loss from EBIC-poor regions related to the Rb aggregates.)

To understand the crystal structure of the Rb clusters, we used a synchrotron-based nanodiffraction technique to enable detection of the secondary phase locally (Fig. 4F). (See figs. S5 and S18 for XRD of other possible precursor phases and Rb perovskites.) The small peak at 27.48° belongs to the $RbPbI_3$ phase. Scanning x-ray Bragg diffraction microscopy (SXDM; beam spot size ~150 nm) was then used to map the low- and high-EBIC regions at the $RbPbI_3$ Bragg angle ($2\theta = 27.48°$) to understand the spatial distribution of this phase (Fig. 4, G and H). With this nanodiffraction setup, the (212) $RbPbI_3$ crystal planes must be oriented out of plane to be detectable. Although only part of the Rb clusters met this criterion and diffracted in area 1, the SXDM maps exhibited the presence of the secondary phase $RbPbI_3$ in the Rb-rich aggregates, whereas no $RbPbI_3$ diffraction was detected in the high-EBIC area 2. Cross-sectional EBIC (Fig. 4I) and the corresponding secondary electron/backscattered electron microscopy (SE/BSE) and energy-dispersive x-ray spectroscopy (EDX) images suggested that Rb aggregates likely nucleated and formed near the TiO_2 interface, and that the aggregate itself was EBIC-inactive and current-blocking.

Together, these data suggest that Rb aggregates were optoelectronically inactive, current-blocking, possibly recombination-active, and detrimental to device performance. Thus, all of the samples showed room for improved performance by addressing alkali-rich precipitates, with the largest potential current gains available in the samples with 5% Rb-I/Br (8% relative; fig. S17). Note that this detrimental impact occurs in parallel to any advantageous effect on halide homogenization caused by RbI and CsI addition. This work helps to elucidate the limitations of adding these alkali metal halides.

REFERENCES AND NOTES

1. N. J. Jeon *et al.*, *Nature* **517**, 476–480 (2015).
2. D. Bi *et al.*, *Sci. Adv.* **2**, e1501170 (2016).
3. W. S. Yang *et al.*, *Science* **356**, 1376–1379 (2017).
4. J.-P. Correa-Baena *et al.*, *Science* **358**, 739–744 (2017).
5. T. J. Jacobsson *et al.*, *J. Am. Chem. Soc.* **138**, 10331–10343 (2016).
6. J.-W. Lee *et al.*, *Adv. Energy Mater.* **5**, 1501310 (2015).
7. C. Yi *et al.*, *Energy Environ. Sci.* **9**, 656–662 (2016).
8. M. Saliba *et al.*, *Energy Environ. Sci.* **9**, 1989–1997 (2016).
9. N. Pellet *et al.*, *Angew. Chem. Int. Ed.* **53**, 3151–3157 (2014).
10. G. E. Eperon *et al.*, *Energy Environ. Sci.* **7**, 982–988 (2014).
11. M. Saliba *et al.*, *Science* **354**, 206–209 (2016).
12. M. Zhang *et al.*, *ACS Energy Lett.* **2**, 438–444 (2017).
13. S.-H. Turren-Cruz *et al.*, *Energy Environ. Sci.* **11**, 78–86 (2018).
14. T. Bu *et al.*, *Energy Environ. Sci.* **10**, 2509–2515 (2017).
15. M. Abdi-Jalebi *et al.*, *Nature* **555**, 497–501 (2018).
16. J. W. Lee, D. J. Seol, A. N. Cho, N. G. Park, *Adv. Mater.* **26**, 4991–4998 (2014).
17. W. Tress, *Adv. Energy Mater.* **7**, 1602358 (2017).
18. J. Zhao *et al.*, *Sci. Adv.* **3**, o5616 (2017).
19. C. Roldán-Carmona *et al.*, *Energy Environ. Sci.* **8**, 3550–3556 (2015).
20. T. Duong *et al.*, *Adv. Energy Mater.* **7**, 1700228 (2017).
21. D. J. Kubicki *et al.*, *J. Am. Chem. Soc.* **139**, 14173–14180 (2017).
22. Z. Tang *et al.*, *Sci. Rep.* **7**, 12183 (2017).
23. H. Demers *et al.*, *Scanning* **33**, 135–146 (2011).

ACKNOWLEDGMENTS

We thank P. Parikh for FIB sample preparation. **Funding:** Supported by the U.S. Department of Energy (DOE) EERE Postdoctoral Research Award (J.-P.C.-B); NSF grant CBET-1605495 (T.B.); Skoltech grant 1913/R as part of the Skoltech NGP Program (T.B., J.-P.C.-B., N.T.P.H., and S.W.); NSF grant DMR-1507803 (J.S., T.W., and L.H.); NSF grant GRFP 1122374 (M.A.J.); DOE grant DE-SC0001088 (L.N. and M.G.B.); California Energy Commission Advance Breakthrough EPC-16-050 (Y.L., S.W., Y.S.M., and D.P.F.); Hellman Fellowship (X.L. and D.P.F.); DOE grant DE-AC02-06CH11357 (Center for Nanoscale Materials and Advanced Photon Source, both Office of Science user facilities); NSF grant CHE-1338173 (TEM work at UC, Irvine, IMRI); and San Diego Nanotechnology Infrastructure with NSF grant ECCS-1542148 (FIB and EBIC).
Author contributions: J.-P.C.-B. and T.B. conceived and designed the overall project; J.-P.C.-B. conducted SEM and XRD experiments, and prepared the perovskite devices; J.-P.C.-B., M.A.J., J.R.P., B.L., N.T.P.H., and S.W. conducted the initial synchrotron measurement (n-XRF); D.P.F., X.L., and Y.L. conducted follow-up n-XRF, XBIC, and SXDM experiments; T.M.B., S.W., Y.L., Y.S.M., and D.P.F. conducted the EBIC measurements; S.W. and Y.S.M. conducted the TEM measurements; J.S., T.W., and L.H. conducted confocal transient absorption microscopy for mapping; L.N. and M.G.B. conducted the PL measurements; T.B., D.P.F., and J.-P.C.-B. directed and supervised the research; J.-P.C.-B. and Y.L. wrote the first draft of the paper; and all authors contributed to the discussion and writing of the paper. **Competing interests:** The authors declare no competing financial interests. **Data and materials availability:** All data are available in the manuscript or the supplementary materials.

SUPPLEMENTARY MATERIALS

www.sciencemag.org/content/363/6427/627/suppl/DC1
Materials and Methods
Figs. S1 to S18
Tables S1 to S3
References (*24*–*34*)

23 April 2018; resubmitted 1 November 2018
Accepted 2 January 2019
10.1126/science.aah5065

Homogenized halides and alkali cation segregation in alloyed organic-inorganic perovskites

Juan-Pablo Correa-Baena, Yanqi Luo, Thomas M. Brenner, Jordan Snaider, Shijing Sun, Xueying Li, Mallory A. Jensen, Noor Titan Putri Hartono, Lea Nienhaus, Sarah Wieghold, Jeremy R. Poindexter, Shen Wang, Ying Shirley Meng, Ti Wang, Barry Lai, Martin V. Holt, Zhonghou Cai, Moungi G. Bawendi, Libai Huang, Tonio Buonassisi and David P. Fenning

Science **363** (6427), 627-631.
DOI: 10.1126/science.aah5065

Advantages of adding just enough alkalis

For organic-inorganic hybrid solar cells, addition of cesium or rubidium cations can improve power conversion efficiency. Correa-Baena *et al.* used nanoscale x-ray fluorescence imaging to show that the addition of metal cations at low concentrations homogenized the distribution of bromide and iodide anions and also increased charge-carrier lifetimes. However, at high concentrations, aggregation and cluster formation led to increased charge recombination.

Science, this issue p. 627